Compact Lithium Niobate Michelson Interferometer Modulators Based on Spiral Waveguides

Amr O. Ghoname, *Graduate Student Member, IEEE*, Ahmed E. Hassanien, Lynford L. Goddard, *Senior Member, IEEE*, and Songbin Gong, *Senior Member, IEEE*

***Abstract*—We demonstrate ultra-compact and highly efficient electro-optic Michelson interferometer modulators on thin film lithium niobate based on spiral-shaped waveguides. The modulator utilizes the in-plane isotropy of the Z-cut lithium niobate refractive index to achieve space-efficient spiral waveguides that are modulated using bottom and top electrodes. Monolithic optical rib waveguides are achieved using dry etching of lithium niobate with bottom and top cladding layers made of silicon dioxide and SU-8 polymer, respectively. The proposed modulator requires a total area of 175 $\times$ 175 μm^2 to accommodate a 9-mm long waveguide, owing to the optimized design of the spiral inner radius and the gap between adjacent turns. The vertical distance between electrodes is engineered to achieve a half-wave-voltage-length product ($V_\pi L$) less than 2.02 V.cm with low optical propagation loss of 1.3 dB/cm. The 3-dB electro-optic bandwidth of the fabricated modulators varied between 4.2 GHz and 17.8 GHz for total spiral lengths of 9 mm and 1.2 mm, respectively. The compact modulator architecture fulfills the pressing demand for high-density photonic integrated circuits in modern data centers and telecommunication networks.**

***Index Terms*—Electro-optic modulator, high-density, photonic integrated circuits, spiral waveguides, thin film lithium niobate.**

I. Introduction

RECENT decades have witnessed an ever-increasing demand for highly-integrated photonic systems that can realize various complex functionalities while making the most efficient use of the on-chip real estate [1]. Among different photonic system components, electro-optic modulators (EOMs) are considered the most attractive building blocks, essential for a wide area of emerging applications including modern telecommunication networks [2], high-traffic data centers [3], quantum photonics [4], and optical sensing applications [5]. Compact and high-performance EOMs that can maintain low driving voltages and optical insertion loss while operating at high data rates are required to meet the progressive technology needs of such applications.

Lithium niobate (LN) has been widely adopted in its traditional bulk form as a major commercial platform for EOMs, due to its strong electro-optic (EO) coefficient, high refractive index, and low optical absorption loss within a wide infrared range [6]. However, bulk modulators suffer from low integration density as well as low modulation efficiency due to the large optical mode size in the formed weakly guiding waveguides and the subsequent need to place the modulating electrodes apart from the waveguides to minimize propagation loss. Therefore, several integrated photonic platforms were adopted to enhance the scalability of EO modulators such as silicon-on-insulator (SOI) [7], indium phosphide [8], silicon nitride [9], and polymers [10], with particular interest in the silicon photonics platform due to its compatibility with complementary metal oxide semiconductor (CMOS) technology. Nevertheless, the non-ideal EO characteristics of these platforms challenged their ability to achieve the aforementioned modulator performance aspects simultaneously. Leveraging the recent advances in nanofabrication techniques, the thin film lithium niobate (TFLN) platform has recently emerged and become a superior candidate for combining the excellent LN material features with high integration capabilities and good confinement of optical modes [11].

A wide range of non-resonant EOMs with promising performance have been successfully demonstrated on the TFLN platform based on the conventional Mach-Zehnder modulator (MZM) configuration [12], [13], [14]. They could feature low half-wave-voltage-length products ($V_\pi L$), in the range of 2.1 to 2.5 V.cm, low optical waveguide loss, less than 0.3 dB/cm, and wide EO bandwidths, up to 100 GHz for traveling-wave modulators [11]. Such non-resonant LN modulators are typically implemented on X/Y cut substrates to ease the fabrication process as well as the traveling-wave modulator design by using coplanar wave electrodes on both sides of waveguides. However, this design requires long straight waveguides that run perpendicular to the in-plane Z crystal axis to harness the EO effect of LN ($r_{33} \approx 31$ pm/V). Thus, it hinders the usage of bent or spiral waveguides that could achieve space-efficient modulators [15], [16], [17]. Although resonant modulators such as microring resonators [18], race-track resonators [19], or photonic crystals [20] could achieve more compact footprints, they are very sensitive to temperature and fabrication variations due to their narrow optical bandwidth.

Manuscript received 31 January 2024; revised 8 April 2024; accepted 14 April 2024. Date of publication 19 April 2024; date of current version 1 May 2024. This work was supported by the National Aeronautics and Space Administration under contract 80NSSC17K052. *(Corresponding author: Amr O. Ghoname.)*

Amr O. Ghoname, Lynford L. Goddard, and Songbin Gong are with the Department of Electrical and Computer Engineering, University of Illinois at Urbana-Champaign, Urbana, IL 61801 USA (e-mail: ghoname2@illinois.edu; lgoddard@illinois.edu; songbin@illinois.edu).

Ahmed E. Hassanien was with the University of Illinois at Urbana-Champaign, Urbana, IL 61801 USA. He is now with the Skyworks Solutions Inc, Irvine, CA 92617 USA (e-mail: ahmed.e.hassanien@gmail.com).

Color versions of one or more figures in this article are available at https://doi.org/10.1109/JSTQE.2024.3391693.

Digital Object Identifier 10.1109/JSTQE.2024.3391693

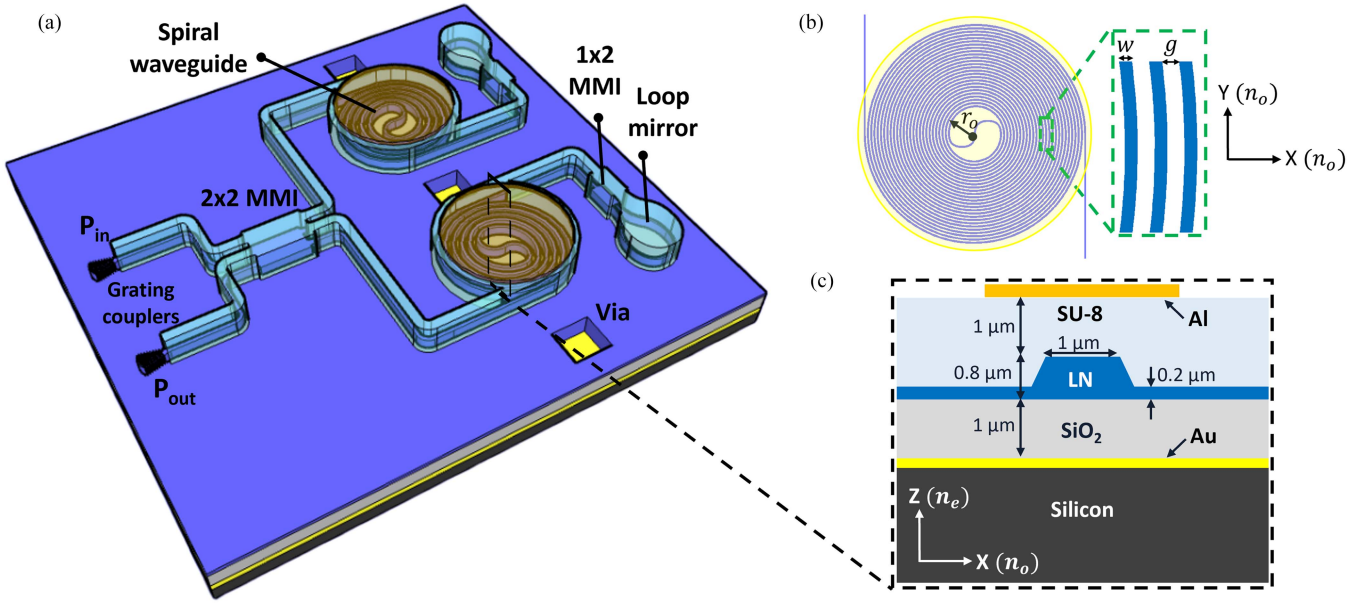

Fig. 1. (a) 3-D schematic of the proposed spiral MIM on thin film Z-cut LN. (b) Top-view of the Archimedean spiral waveguide showing its relevant design parameters; $w = 1\,\mu$m, $g = 1.5\,\mu$m, $r_o = 20\,\mu$m. (c) Cross-section of the implemented waveguide showing different materials of the stack and their vertical dimensions. n_o and n_e are the ordinary and extra-ordinary refractive indices of LN, respectively.

Recently, a new family of spiral non-resonant EOMs was presented on the Z-cut TFLN platform with ultra-compact footprint [21], [22], [23]. In Z-cut, the LN refractive index is isotropic in plane, allowing for a flexible photonic circuit design with spiral-shaped optical waveguides that can be efficiently modulated using top and bottom electrodes [11]. Spiral MZMs were presented with a miniaturized on-chip size wrapping a 2-cm long waveguide into a 300×300 μm^2 area [21]. The main drawback in these Z-cut EO modulators is the limited modulation bandwidth, restricted by the R-C (resistance-capacitance) electrical limit, because the RF electrodes are considered lumped in this configuration [19], [21]. As a result, the modulation efficiency ($V_\pi L$) is also compromised because reducing the gap between optical waveguides and RF electrodes to enhance the efficiency would negatively affect the EO bandwidth due to the increased device capacitance. The minimum demonstrated $V_\pi L$ for MZM modulators was 6.4 V.cm using single arm modulation.

In this work, we demonstrate a Michelson interferometer modulator (MIM) based on the spiral configuration on Z-cut LN. With reflective mirrors at both ends of Michelson arms, the interaction length between optical and RF electric fields doubles within the same waveguide physical length. As a result, the fabricated MIM devices could achieve $V_\pi L$ down to 1.88 V.cm by simultaneous modulation of two spirals in a push-pull configuration. Several modulators with total waveguide lengths ranging from 9 mm to 1.2 mm could fit into circular spirals with a maximum radius of 175 μm and 75 μm, respectively. The resulting 3-dB EO bandwidth varied between 4.2 GHz to 17.8 GHz according to the R-C limit, that arises from the device capacitance and the 50 Ω driving resistance of the measuring instruments, as well as the optical to RF phase mismatch limit. Owing to their improved $V_\pi L$, the spiral MIMs achieve wider bandwidth compared to MZM designs with the same modulating voltage due to their smaller capacitance, resulting in a better voltage-bandwidth figure of merit (BW/V_π) [11]. Further incorporating the optical modulators with integrated electronic front-end circuits could achieve broader RC modulation bandwidths by lowering the modulator driving resistance in a custom-designed circuit interface.

II. Modulator Design

Fig. 1(a) shows a three-dimensional (3-D) schematic of the spiral MIM structure. Two grating couplers are used for input/output light coupling to/from the photonic chip [24]. Input light is split using a 2 × 2 multimode interference (MMI) waveguide into two Michelson arms that end with reflective loop mirrors. The spiral optical waveguides in both Michelson arms are achieved by connecting two Archimedean spirals using an S-curved waveguide located at the spiral center, as shown in Fig. 1(b) [17], [21]. The modulator was implemented on Z-cut LN on insulator (LNOI) wafer with the stack shown in Fig. 1(c). The initial stack, prepared by NanoLN, was composed of a silicon handle layer, a metallization gold (Au) layer with a total thickness of 140 nm including top and bottom chromium (Cr) adhesion layers, 1 μm silicon dioxide (SiO_2) bottom cladding layer, and 800 nm thick Z-cut LN. The optical waveguiding structures were patterned on LN before covering the devices with a top cladding layer made of SU-8 polymer and depositing 200 nm layer of aluminum (Al) top electrodes above the modulating spirals. The SU-8 polymer was chosen because it can be spin-coated over the LN structures providing a highly uniform cladding layer with good insulation properties and flexible thickness [21], [25]. In addition, it has good RF and optical properties ($\varepsilon_r \approx 3$ and $n_r \approx 1.57$ at 1500 nm) [26], providing strong optical mode guiding due to its high index

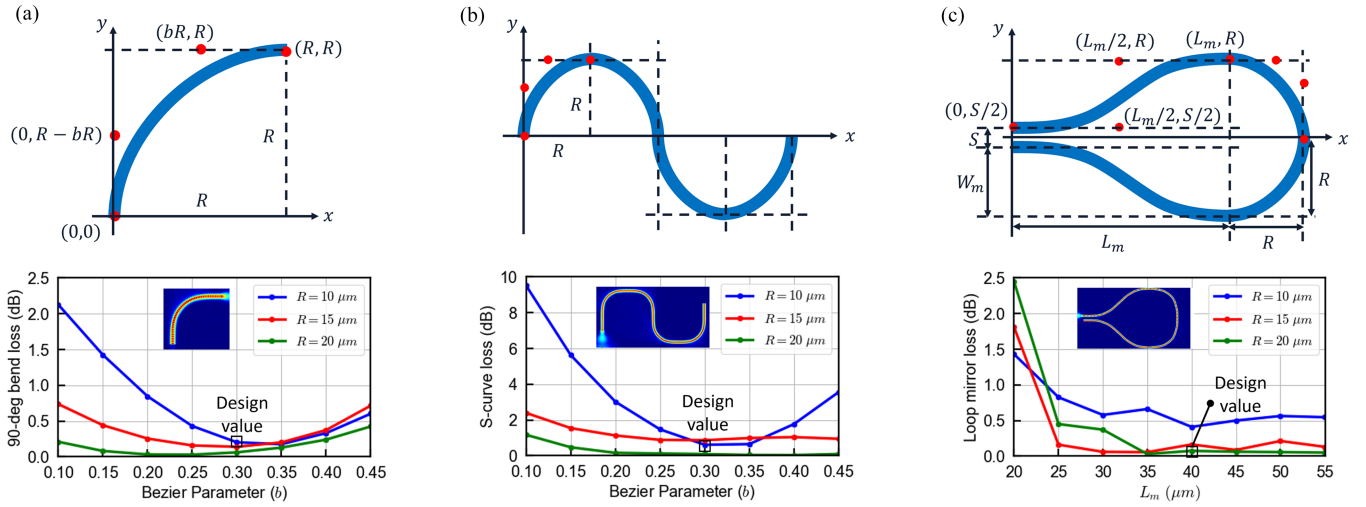

Fig. 2. Design structure and simulated optical loss of different bending shapes in the MIM design: (a) Single 90-deg cubic Bezier bend, indicating the selected design point at $b = 0.3$ and $R = 10\,\mu$m, (b) Connecting S-curve between Archimedean spirals formed by four 90-deg bends, indicating the same design point, (c) Loop mirror formed by four cubic Bezier curves, indicating the selected design point at $L_m = 40\,\mu$m and $R = 20\,\mu$m.

contrast with LN. Al metal was selected for top electrodes as it features lower propagation loss of the optical mode at 1550 nm compared to other metals, as evident from optical mode simulations. Although Au exhibits similar loss to Al, it requires a Cr adhesion layer that significantly increases the optical loss. During wafer preparation, Al was not available as a bottom metal layer. Thus, lower achievable waveguide loss is expected for our devices by using Al bottom electrodes in the future. Different parameters of the optical and RF paths are optimized to improve the MIM performance including insertion loss, modulation efficiency, and EO bandwidth.

Initially, the design dimensions of the passive optical components were optimized using Lumerical simulation tools. The transverse magnetic (TM) mode was adopted such that the optical mode polarization is parallel to the electric field along the Z crystal to harness the strong r_{33} EO coefficient of LN. The TM mode was simulated in rib waveguides with a bottom slab and a slanted sidewall angle of 70°, which was characterized for our fabrication process. We chose a waveguide width (w) of 1 μm to minimize the propagation absorptive loss from metal electrodes to 0.2 dB/cm for 1 μm top cladding thickness. A slab thickness of 200 nm was chosen to minimize the scattering loss by reducing the optical mode overlap with rough etched surfaces, while still supporting the TM mode in the waveguide. The simulated mode effective and group indices at 1550 nm are $n_{eff} = 1.93$ and $n_g = 2.3$, respectively. The MMI waveguides were designed based on the self-image theory [27], such that the MMI length is set at the position of the first 2-fold images, expressed as $L_{MMI} = 3L_\pi/8$ for 1×2 MMI, and $L_{MMI} = L_\pi/2$ for 2×2 MMI, where L_π is the beating length of the two lowest-order modes. The beating length is calculated as $L_\pi = 4nW_e^2/3\lambda_o$, where n is the MMI guiding index, W_e is the MMI effective width and λ_o is the light wavelength. To minimize the MMI size while achieving low insertion loss, we chose W_e as 6.5 μm and 9 μm for the 1×2 MMI and 2×2 MMI, respectively. After optimizing the structure using Lumerical finite difference time domain (FDTD) simulations, a 3-dB splitting ratio was achieved

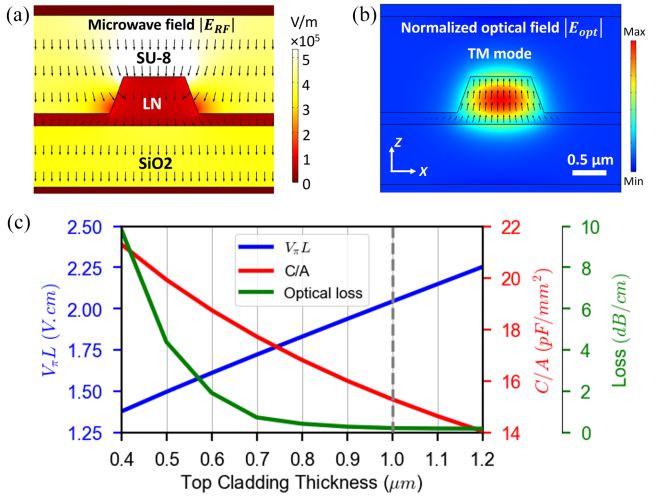

Fig. 3. Simulated (a) microwave and (b) optical electric field distributions in the Z-cut EO modulator. (c) Simulation of $V_\pi L$, capacitance per unit area and optical loss vs top cladding thickness, showing different trade-offs in the RF path design. Selected operating point at 1 μm is indicated by the vertical dashed line.

for both MMI waveguides with 0.25 dB excess loss at 1550 nm, using L_{MMI} of 31 μm for the 1×2 MMI and 80 μm for the 2×2 MMI. The separation between the output waveguides of MMI waveguides are 3.6 μm and 3 μm for the 1×2 MMI and 2×2 MMI, respectively.

The size of the spiral waveguides and loop mirrors was optimized to minimize the modulator footprint. The gap between the spiral turns (g) was selected as 1.5 μm to reduce the evanescent mode coupling coefficient between adjacent waveguides. The S-curve connecting the two spiral waveguides consists of four 90° bends as shown in Fig. 2(b). The bends' curvature was designed using Bezier curves that have been shown to provide low bending loss compared to circular bends in silicon photonics platforms [28]. Each bend is described by a four-point cubic Bezier curve, whose coordinates are defined by the bend radius

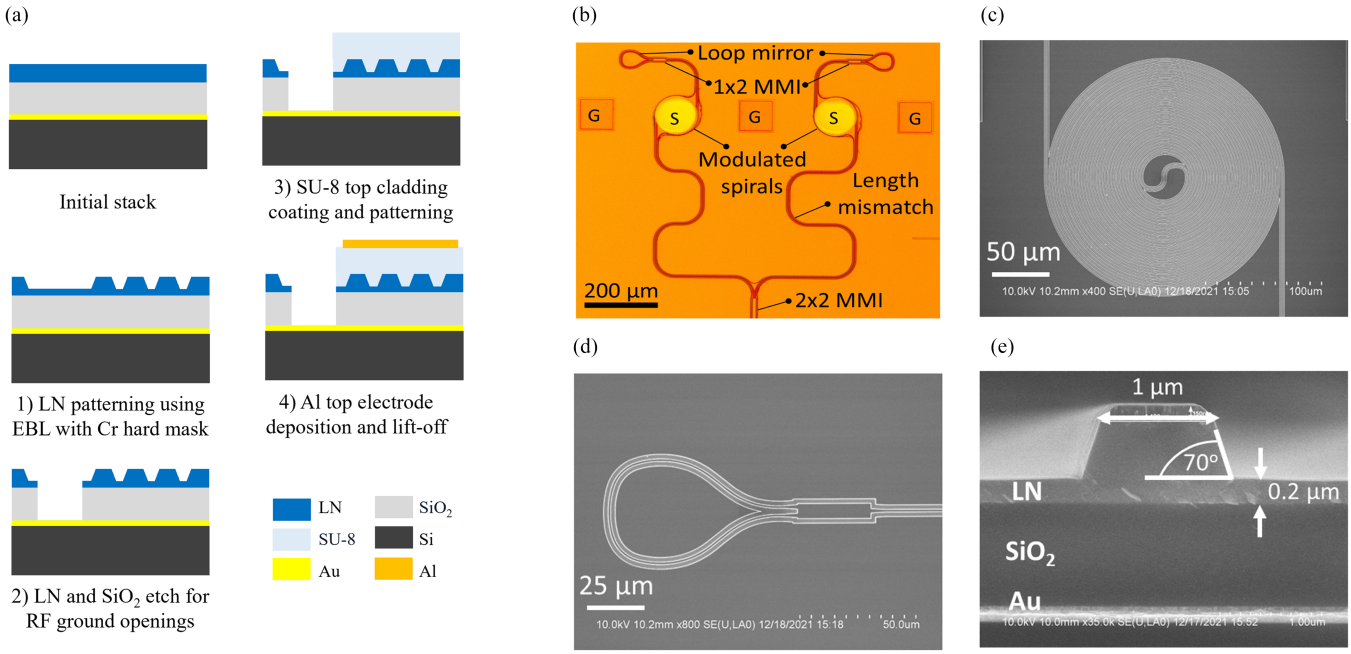

Fig. 4. (a) Detailed fabrication process steps of MIM on Z-cut LN. (b) Microscope image of the final fabricated MIM. SEM images of the fabricated components before adding the top SU-8 cladding and electrode layers showing: (c) Top-view of the spiral waveguide; (d) Top-view of the loop mirror; (e) Cross-sectional view of one optical waveguide showing 70° sidewall angle of the dry etching recipe.

(R) and the Bezier parameter (b) as shown in Fig. 2(a). Based on sweep simulations, the bend parameters were selected as $b = 0.3$ and $R = 10\,\mu$m, realizing a total bending loss of 0.2 dB for the 90° bend and 0.6 dB for the S-curve at 1550 nm, as shown in FDTD simulation results in Fig. 2(a) and (b), respectively. The design results in a minimum radius of the inner S-curve; $r_o = 20\,\mu$m. The loop mirrors were also designed using Bezier bends, such that each mirror consists of four cubic Bezier curves. Two of the curves are 90° bends with similar design parameters as aforementioned. The other two curves translate the light path between the 1 × 2 MMI ports and the 90° bends. They can be described by four-point Bezier curves whose coordinates are defined by the curve length (L_m) and width (W_m), as shown in Fig. 2(c). The separation between the loop mirror input and output waveguides (S) is defined by the 1 × 2 MMI design as 3.6 μm. Thus, W_m is related to the 90° bend radius as $W_m = R - S/2$. As L_m increases, the 90° bend loss dominates over the other translating Bezier curve loss. The loop mirror was simulated at swept L_m and R values, resulting in a total loss of 0.07 dB loss at 1550 nm with $L_m = 40\,\mu$m and $R = 20\,\mu$m. Thus, the total loop mirror design size becomes 60 μm × 40 μm. In general, a lower insertion loss of each optical component can be achieved at larger dimensions, yet at the expense of the total device area and capacitance.

Subsequently, the RF modulation path is studied by simulating the microwave electric field and device capacitance at different electrode gaps using COMSOL Multiphysics. The electrode gap is swept by varying the top SU-8 cladding layer thickness, which can be easily controlled in practice by the spin coating speed. As thickness increases, the optical loss and capacitance per unit area decrease, resulting in a higher EO bandwidth, but at the expense of reduced efficiency and higher $V_\pi L$. The simulated microwave and optical electric field distributions are shown in Fig. 3(a) and (b), respectively, while the design tradeoffs are depicted in the simulation results in Fig. 3(c). An SU-8 top cladding thickness of 1 μm was selected for MIM implementation, resulting in a simulated $V_\pi L$ of 2.04 V.cm.

III. Modulator Implementation and Characterization

A. Fabrication Process

The device is implemented using four lithography steps as shown in the fabrication process flow in Fig. 4(a). First, the LN waveguides were realized using dry etching with a Cr hard mask. A thin Cr layer was sputtered with an optimized thickness of 200 nm given the selectivity of the etching process and the LN etch depth (600 nm). Next, a photoresist layer was patterned using electron beam lithography (EBL). In an inductively coupled plasma reactive ion etching (ICP-RIE) chamber, Cr and LN were etched using chlorine-based ($Cl_2 + O_2$) plasma and fluorine-based (CHF_3 + Ar) plasma, respectively [29]. The Cr mask was then removed using wet etching and a piranha cleaning step was performed to remove the redeposition from dry etch and other contaminants. Second, openings to the bottom Au ground electrode were defined using optical lithography and dry etching of the LN slab (200 nm) and SiO_2 layer. Third, the SU-8 top cladding layer was spin-coated and patterned to cover all optical components except for the input and output grating couplers. To ensure stable properties, the SU-8 was hard baked at 150 °C. Fourth, the top Al layer was sputtered and patterned above the modulated spirals using the lift-off process.

Fig. 4(b) shows a top-view optical microscope image of the fabricated modulator. Long connecting waveguides are used to

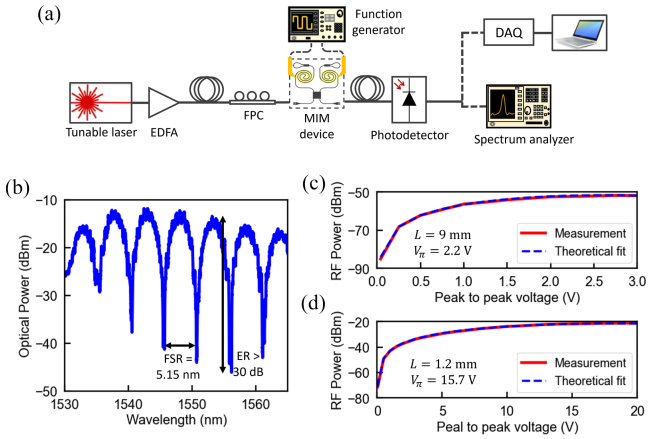

Fig. 5. (a) Experimental setup to measure the optical response and modulation efficiency of the MIM. (b) Measured optical spectrum of unbalanced MIM. (c), (d) Measured RF power vs applied voltage and fundamental Bessel function fit to obtain V_π for the 9 mm and 1.2 mm devices, respectively.

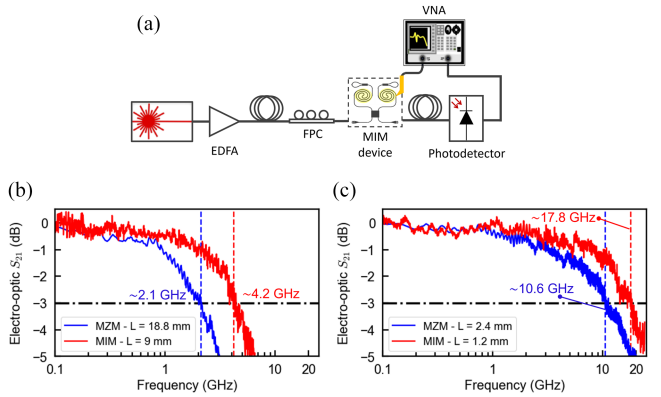

Fig. 6. (a) Experimental setup to characterize the frequency response of the MIM using VNA. (b), (c) Measured EO S_{21} of the 9 mm and 1.2 mm MIM devices (red lines) showing their 3-dB bandwidth and comparing them to 18.8 mm and 2.4 mm MZM devices with similar V_π (blue lines).

accommodate the minimum distance between the optical and RF probes used in the measurements. Moreover, waveguide bending is used in both Michelson arms to achieve a length mismatch for optimum modulator operation at the quadrature point. Top-view scanning electron microscope (SEM) images for the spiral waveguide and loop mirror, before adding the SU-8 and top metal layer, are displayed in Fig. 4(c) and (d), respectively. Cross-sectional SEM of the optical waveguide is viewed in Fig. 4(e), showing a sidewall angle of 70°, realized using the dry etching process.

B. Experimental Results and Discussion

The adopted design and fabrication process were used to implement multiple MIM devices with different number of spiral turns resulting in total lengths of 9 mm, 5 mm, 2.8 mm, and 1.2 mm. First, the optical response of the unbalanced MIM was measured using the setup shown in Fig. 5(a). Using grating couplers, the input light was vertically coupled from a tunable laser source (Santec 710 TSL) into multiple on-chip modulators. A fiber polarization controller (FPC) was used to adjust the input polarization to the TM mode and an erbium-doped fiber optical amplifier (EDFA) was used to boost the input signal power. The transmission spectrum was measured at swept wavelengths using a high-speed photodetector that converted the optical output to electrical signals, which were read out using a PC-controlled data acquisition card (DAQ). The measured spectrum of the 1.2 mm modulator is plotted in Fig. 5(b), showing an extinction ratio $>$ 30 dB and a free spectral range (FSR) of 5.15 nm due to a length mismatch of ($\Delta L = 100\,\mu$m) between Michelson arms. The modulator on-chip insertion loss and fiber-to-chip coupling loss were measured as ~6.2 dB and ~13 dB per each grating coupler, respectively. The waveguide propagation loss with top and bottom electrodes was separately measured as ~1.3 dB/cm using a ring resonator design with 40 μm radius [21]. According to the previously discussed FDTD simulations, the metal induced waveguide propagation loss was estimated as 0.2 dB/cm, and the total insertion loss of different on-chip components, including the bending loss, the loop mirror loss, and the MMI excess loss, can be calculated as ~2.7 dB. The excess on-chip loss compared to the simulation value is attributed to the scattering loss from sidewall surface roughness which can be minimized by improving the LN dry etching and post-cleaning processes. Furthermore, the fiber-to-chip loss can be reduced by using end-fire coupling to avoid the high grating coupler loss, attributed to fabrication tolerances in the grating period and etching depth.

Next, the half-wave voltage (V_π) was measured for each MIM design to evaluate the modulation efficiency. Usually, V_π is measured by observing the modulator transmission while applying a linearly changing DC modulating voltage signal to the electrodes. Nevertheless, it was observed that the DC response of the proposed Z-cut LN modulators is very weak and unstable [18], [21]. This behavior is attributed to the space charge effects in TFLN including the redistribution of mobile carriers in the device structure that may shield the applied electric field [11], [30]. Consequently, V_π was measured at high frequency by applying a 1 MHz sinusoidal modulating signal and observing the output power at the fundamental frequency using a spectrum analyzer as shown in the measurement setup in Fig. 5(a). According to the theoretical analysis of MIM output spectrum with a sinusoidal input, the relative output optical power is expressed as [31]:

$$P_{out}^{opt} = \frac{P_{in}^{opt} T}{2} \{1 + \cos\left[|\Delta\varphi_n| \cos\left(\omega_{RF} t\right)\right] \cos \Delta\varphi_L + \sin\left[|\Delta\varphi_n| \cos\left(\omega_{RF} t\right)\right] \sin \Delta\varphi_L\} \quad (1)$$

where P_{in}^{opt} is the input optical power, T is the transmission coefficient, $\Delta\varphi_L$ is the phase shift between Michelson arms due to length and other non-ideal mismatches, and $\Delta\varphi_n$ is the phase shift due to index perturbation caused by the RF modulating signal. $\Delta\varphi_n = |\Delta\varphi_n| \cos(\omega_{RF} t)$, where ω_{RF} is the angular frequency of the sinusoidal input and $|\Delta\varphi_n|$ is the phase shift amplitude calculated as; $|\Delta\varphi_n| = \pi V_{pp}/2V_\pi$, where V_{pp} is the peak-to-peak input voltage. Applying Jacobi-Anger expansion to the above relation allows us to analyze the harmonic contents of the output power and reach the following expression for the

TABLE I
PERFORMANCE SUMMARY OF THE SPIRAL MIMS AND COMPARISON TO REPORTED MIMS ON LNOI PLATFORM

Device # / Reference	Modulation length (L)	Effective on-chip length (L_{eff})[a]	V_π (V)	$V_\pi L$ (V.cm)[b]	3-dB EO bandwidth (GHz)
1	9 mm	175 µm	2.2	1.98	4.2
2	5 mm	135 µm	3.9	1.95	6.7
3	2.8 mm	105 µm	7.2	2.02	11.2
4	1.2 mm	75 µm	15.7	1.88	17.8
[32]	1 mm	1 mm	14	1.4	12
[33][c]	1 mm	1 mm	12	1.2	17.5
[34][d]	600 µm	600 µm	17.8	1.06	40

Devices 1, 2, 3, and 4 are spiral MIMs demonstrated in this work.
[a] L_{eff} represents the longest on-chip dimension of the phase shifter, i.e., the spiral waveguide's outer diameter or the straight waveguide's total length (L).
[b] $V_\pi L$ is calculated based on the total modulation length (L).
[c] MIM was implemented on hybrid SOI/LNOI platform.
[d] MIM was implemented on hybrid SRN/LNOI platform and utilizes Bragg reflectors instead of loop mirrors to enhance the traveling-wave bandwidth.

power magnitude at the fundamental harmonic:

$$P_1^{opt} = P_{in}^{opt} T \times J_1\left(\frac{\pi V_{pp}}{2V_\pi}\right) \sin \Delta\varphi_L \tag{2}$$

where J_1 is the 1st order Bessel function of the first kind. Because the output voltage of the photodetector is proportional to the optical power, the measured RF power using the spectrum analyzer can be expressed as:

$$P_1^{RF} = C \times \left[J_1\left(\frac{\pi V_{pp}}{2V_\pi}\right) \sin \Delta\varphi_L \right]^2 \tag{3}$$

where C is a constant representing the photodetector responsivity and other power conversion losses in the measurement setup. As a result, V_π is calculated by fitting the measured fundamental RF power at swept input voltages to (3). The fitted curves of the 9 mm and 1.2 mm devices are shown in Fig. 5(c) and (d) respectively, indicating the extracted V_π values of 2.2 V and 15.7 V for both devices. That corresponds to $V_\pi L$ values of 1.98 and 1.88, respectively, which are in good agreement with the simulation result. In order to maximize the output power, the modulator is optimally operated by tuning the input laser wavelength to the quadrature point at -3 dB optical transmission ($\Delta\varphi_L = \pi/2$). DC voltage tuning could not be used for modulator biasing due to its weak response. In practice, thermo-optic phase shifters could be added to the modulator design to overcome this complication and achieve efficient and stable biasing [35].

Finally, the small signal EO frequency response of the MIM was characterized using a 40 GHz two-port vector network analyzer (VNA; Agilent N5230A) as shown in the measurement setup in Fig. 6(a). While port 1 of the VNA is connected to one of the RF electrodes to apply the modulating signal, port 2 is connected to the output of the photodetector that has an extended bandwidth of up to 40 GHz (Thorlabs RXM40AF). To compare performance regarding EO bandwidth, each MIM device is compared to a spiral MZM device that has a similar V_π (twice the physical length) and was previously implemented using the same fabrication process. Fig. 6(b) and (c) display the measured EO S_{21} response of the MIM devices (red lines) with a comparison to their MZM counterparts (blue lines). Demonstrated bandwidths of 4.2 GHz and 17.8 GHz for the 9 mm and 1.2 mm MIMs compare favorably to bandwidths of 2.1 GHz and 10.6 GHz for the 18.8 mm and 2.4 mm MZMs. Increasing the MIM phase shifter length achieves lower V_π, yet at the expense of reduced bandwidth. Moreover, MIM designs demonstrate bandwidth enhancement compared to MZMs because they feature lower capacitances, having half modulation lengths and more compact electrode sizes. The smaller size relaxes the R-C time constant, which is the main bandwidth limitation of the spiral Z-cut modulators with lumped electrode configuration. While the capacitance (C) of the device is defined by the device area and the waveguide-to-electrode gap in the RF path design, the resistance (R) is limited in our measurements by the 50 Ω impedance of the VNA drive. Thus, the R-C bandwidth limit can be pushed to much higher values upon further integration of the optical modulators with electronic integrated driving circuits, where a lower output interface resistance could be custom-achieved. It is worth noting that another bandwidth limitation arises from the phase mismatch between the optical and RF fields through the spiral waveguide. As the optical signal experiences different phase shifts within the waveguide propagation time, the average accumulated phase could be affected at high RF frequencies. The phase mismatch limit can be evaluated by replacing the instantaneous sinusoidal phase ($\Delta\varphi_n$) in (1) with the time-varying average of the accumulated phase through the waveguide. After applying Jacobi-Anger expansion and solving numerically for the fundamental harmonic, the 3-dB bandwidth can be estimated from $f_{3-dB} = \mu/\tau$, where τ is the light propagation time in the waveguide and $\mu \sim 0.6$ for small signal modulation. Other limitations could also arise from the non-ideal properties of the stack materials including the loss tangent of SiO_2 and SU-8 dielectric materials as well as the reduced conductivity of the deposited thin metal film that may increase the contact resistance between the RF probes and electrodes and reduce the overall bandwidth of the modulators.

Table I summarizes different performance metrics of the four fabricated spiral MIMs and compares them to other reported traveling-wave MIMs on LNOI platform. Hybrid platforms were adopted in [33], where SOI/LNOI system is chosen to benefit from the high scalability and low coupling loss of silicon

photonics, and in [34], where silicon rich nitride (SRN)/LNOI platform is used to achieve short Bragg grating reflectors at the end of Michelson arms to enhance the traveling-wave modulator bandwidth. To compare the footprint size of the spiral phase shifter to conventional straight waveguides, we use another parameter, the effective on-chip length (L_{eff}), which represents the longest dimension of the phase shifter. This length is the spiral outer diameter in our MIM or the same total length (L) of the straight waveguide modulators. Much smaller footprints could be achieved using the spiral MIM compared to previous implementations with a competitive $V_\pi L$; however, the bandwidth becomes R-C limited and scales down at lower V_π in the lumped configuration. In that context, it should be noted that the traveling-wave MIMs have narrower bandwidths compared to traveling-wave MZMs, due to velocity mismatch limitation caused by counter propagation of optical and microwave signals in one of the MIM propagation directions [32], [34]. That contrasts with the spiral configuration, where MIM design achieves wider bandwidth than MZM due to the reduced device capacitance at shorter spiral lengths. It is also worth mentioning that a bandwidth-length trade-off exists in traveling-wave MIMs, as increasing the modulator length to achieve lower V_π would result in lower EO bandwidth due to the microwave loss and velocity mismatch [36], [37]. As a result, the proposed spiral MIM configuration achieves modulation bandwidths on par with the previous MIM implementations while featuring a more compact footprint.

IV. Conclusion

We report a highly compact MIM on thin film Z-cut LN based on spiral configuration. Using top and bottom electrodes, the spiral-shaped waveguides are efficiently modulated, achieving a product of $V_\pi L$ as low as 1.88 V.cm. The modulator utilizes SiO_2 as a bottom cladding and SU-8 to realize a top cladding layer with a controllable thickness and a uniform surface for the top electrodes. The electrodes are considered lumped in the proposed modulators resulting in R-C limited EO bandwidth that varies according to the modulator length and the achievable V_π. We experimentally demonstrated several modulation lengths ranging from 9 mm to 1.2 mm, resulting in high bandwidths of 4.2 GHz up to 17.8 GHz, measured using 50 Ω driving resistance. The spiral configuration could wrap the 9-mm long waveguide into a circular spiral with 175 μm total diameter, allowing for fitting extremely long phase shifters in a miniaturized on-chip area. Therefore, the proposed spiral MIM is an excellent choice for highly integrated photonic circuits, where incorporating a large number of devices within the smallest chip footprint is rigorously needed.

References

[1] D. Marpaung, J. Yao, and J. Capmany, "Integrated microwave photonics," *Nature Photon.*, vol. 13, no. 2, pp. 80–90, Feb. 2019, doi: 10.1038/s41566-018-0310-5.

[2] P. J. Winzer, D. T. Neilson, and A. R. Chraplyvy, "Fiber-optic transmission and networking: The previous 20 and the next 20 years [Invited]," *Opt. Exp.*, vol. 26, no. 18, Sep. 2018, Art. no. 24190, doi: 10.1364/OE.26.024190.

[3] H. Wang et al., "Silicon photonic transceivers for application in data centers," *J. Semicond.*, vol. 41, no. 10, Oct. 2020, Art. no. 101301, doi: 10.1088/1674-4926/41/10/101301.

[4] H. - P. Lo, T. Ikuta, N. Matsuda, T. Honjo, and H. Takesue, "Electro-optic modulators for photonic quantum information processing," *Proc. SPIE*, vol. 11195, 2019, Art. no. 111950P, doi: 10.1117/12.2538667.

[5] L. Duvillaret, S. Rialland, and J. - L. Coutaz, "Electro-optic sensors for electric field measurements I Theoretical comparison among different modulation techniques," *J. Opt. Soc. Amer. B*, vol. 19, no. 11, pp. 2692–2703, Nov. 2002, doi: 10.1364/JOSAB.19.002692.

[6] E. L. Wooten et al., "A review of lithium niobate modulators for fiber-optic communications systems," *IEEE J. Sel. Topics Quantum Electron.*, vol. 6, no. 1, pp. 69–82, Jan./Feb. 2000, doi: 10.1109/2944.826874.

[7] G. T. Reed, G. Mashanovich, F. Y. Gardes, and D. J. Thomson, "Silicon optical modulators," *Nature Photon.*, vol. 4, no. 8, pp. 518–526, Aug. 2010, doi: 10.1038/nphoton.2010.179.

[8] M. Smit, K. Williams, and J. van der Tol, "Past, present, and future of InP-based photonic integration," *APL Photon.*, vol. 4, no. 5, May 2019, Art. no. 050901, doi: 10.1063/1.5087862.

[9] K. Alexander et al., "Nanophotonic Pockels modulators on a silicon nitride platform," *Nature Commun.*, vol. 9, no. 1, Dec. 2018, Art. no. 3444, doi: 10.1038/s41467-018-05846-6.

[10] S. Koeber et al., "Femtojoule electro-optic modulation using a silicon–organic hybrid device," *Light Sci. Appl.*, vol. 4, no. 2, Feb. 2015, Art. no. e255, doi: 10.1038/lsa.2015.28.

[11] D. Zhu et al., "Integrated photonics on thin-film lithium niobate," *Adv. Opt. Photon.*, vol. 13, no. 2, pp. 242–352, Jun. 2021, doi: 10.1364/AOP.411024.

[12] C. Wang et al., "Integrated lithium niobate electro-optic modulators operating at CMOS-compatible voltages," *Nature*, vol. 562, no. 7725, pp. 101–104, Oct. 2018, doi: 10.1038/s41586-018-0551-y.

[13] M. Zhang, C. Wang, P. Kharel, D. Zhu, and M. Lončar, "Integrated lithium niobate electro-optic modulators: When performance meets scalability," *Optica*, vol. 8, no. 5, pp. 652–667, May 2021, doi: 10.1364/OPTICA.415762.

[14] M. Xu et al., "High-performance coherent optical modulators based on thin-film lithium niobate platform," *Nature Commun.*, vol. 11, no. 1, Dec. 2020, Art. no. 3911, doi: 10.1038/s41467-020-17806-0.

[15] B. Ouyang et al., "On-chip silicon Mach–Zehnder interferometer sensor for ultrasound detection," *Opt. Lett.*, vol. 44, no. 8, pp. 1928–1931, Apr. 2019, doi: 10.1364/OL.44.001928.

[16] A. Khachaturian, B. Abiri, and A. Hajimiri, "A compact spiral Mach-Zehnder Interferometer Modulator on SOI process," in *Proc. IEEE 12th Int. Conf. Group IV Photon.*, 2015, pp. 151–152. doi: 10.1109/Group4.2015.7305996.

[17] A. D. Simard, Y. Painchaud, and S. LaRochelle, "Integrated Bragg gratings in spiral waveguides," *Opt. Exp.*, vol. 21, no. 7, pp. 8953–8963, Apr. 2013, doi: 10.1364/OE.21.008953.

[18] M. Bahadori, Y. Yang, A. E. Hassanien, L. L. Goddard, and S. Gong, "Ultra-efficient and fully isotropic monolithic microring modulators in a thin-film lithium niobate photonics platform," *Opt. Exp.*, vol. 28, no. 20, Sep. 2020, Art. no. 29644, doi: 10.1364/OE.400413.

[19] C. Wang, M. Zhang, B. Stern, M. Lipson, and M. Lončar, "Nanophotonic lithium niobate electro-optic modulators," *Opt. Exp.*, vol. 26, no. 2, pp. 1547–1555, Jan. 2018, doi: 10.1364/OE.26.001547.

[20] M. Li et al., "Lithium niobate photonic-crystal electro-optic modulator," *Nature Commun.*, vol. 11, no. 1, Dec. 2020, Art. no. 4123, doi: 10.1038/s41467-020-17950-7.

[21] A. E. Hassanien, A. O. Ghoname, E. Chow, L. L. Goddard, and S. Gong, "Compact MZI modulators on thin film Z-cut lithium niobate," *Opt. Exp.*, vol. 30, no. 3, pp. 4543–4552, Jan. 2022, doi: 10.1364/OE.446665.

[22] A. O. Ghoname, A. E. Hassanien, E. Chow, L. L. Goddard, and S. Gong, "Highly linear lithium niobate Michelson interferometer modulators assisted by spiral Bragg grating reflectors," *Opt. Exp.*, vol. 30, no. 22, pp. 40666–40681, Oct. 2022, doi: 10.1364/OE.472673.

[23] A. O. Ghoname, A. E. Hassanien, E. Chow, L. L. Goddard, and S. Gong, "Spiral waveguide Bragg grating modulator on thin-film Z-cut lithium niobate," *J. Opt. Soc. Amer. B*, vol. 40, no. 5, pp. D38–D43, May 2023, doi: 10.1364/JOSAB.482339.

[24] A. Kar, M. Bahadori, S. Gong, and L. L. Goddard, "Realization of alignment-tolerant grating couplers for Z-cut thin-film lithium niobate," *Opt. Exp.*, vol. 27, no. 11, pp. 15856–15867, May 2019, doi: 10.1364/OE.27.015856.

[25] B. Yang et al., "Fabrication and characterization of small optical ridge waveguides based on SU-8 Polymer," *J. Lightw. Technol.*, vol. 27, no. 18, pp. 4091–4096, Sep. 2009, doi: 10.1109/JLT.2009.2022285.

[26] N. Ghalichechian and K. Sertel, "Permittivity and loss characterization of SU-8 films for mmW and terahertz applications," *IEEE Antennas Wireless Propag. Lett.*, vol. 14, pp. 723–726, 2015, doi: 10.1109/LAWP.2014.2380813.
[27] L. B. Soldano and E. C. M. Pennings, "Optical multi-mode interference devices based on self-imaging: Principles and applications," *J. Lightw. Technol.*, vol. 13, no. 4, pp. 615–627, Apr. 1995, doi: 10.1109/50.372474.
[28] M. Bahadori, M. Nikdast, Q. Cheng, and K. Bergman, "Universal design of waveguide bends in silicon-on-insulator photonics platform," *J. Lightw. Technol.*, vol. 37, no. 13, pp. 3044–3054, Jul. 2019, doi: 10.1109/JLT.2019.2909983.
[29] I. Krasnokutska, J.-L. J. Tambasco, X. Li, and A. Peruzzo, "Ultra-low loss photonic circuits in lithium niobate on insulator," *Opt. Exp.*, vol. 26, no. 2, pp. 897–904, Jan. 2018, doi: 10.1364/OE.26.000897.
[30] J. P. Salvestrini, L. Guilbert, M. Fontana, M. Abarkan, and S. Gille, "Analysis and control of the DC drift in $LiNbO_3$ based Mach–Zehnder modulators," *J. Lightw. Technol.*, vol. 29, no. 10, pp. 1522–1534, May 2011, doi: 10.1109/JLT.2011.2136322.
[31] A. E. Hassanien et al., "Efficient and wideband acousto-optic modulation on thin-film lithium niobate for microwave-to-photonic conversion," *Photon. Res.*, vol. 9, no. 7, pp. 1182–1190, Jul. 2021, doi: 10.1364/PRJ.421612.
[32] J. Jian et al., "High modulation efficiency lithium niobate Michelson interferometer modulator," *Opt. Exp.*, vol. 27, no. 13, pp. 18731–18739, Jun. 2019, doi: 10.1364/OE.27.018731.
[33] M. Xu et al., "Michelson interferometer modulator based on hybrid silicon and lithium niobate platform," *APL Photon.*, vol. 4, no. 10, Oct. 2019, Art. no. 25462, doi: 10.1063/1.5115136.
[34] X. Huang et al., "40 GHz high-efficiency Michelson interferometer modulator on a silicon-rich nitride and thin-film lithium niobate hybrid platform," *Opt. Lett.*, vol. 46, no. 12, pp. 2811–2814, Jun. 2021, doi: 10.1364/OL.425181.
[35] S. Sun et al., "Bias-drift-free Mach–Zehnder modulators based on a heterogeneous silicon and lithium niobate platform," *Photon. Res*, vol. 8, no. 12, pp. 1958–1963, Dec. 2020, doi: 10.1364/PRJ.403167.
[36] J. A. Ibarra Fuste and M. C. Santos Blanco, "Bandwidth–length trade-off figures of merit for electro-optic traveling wave modulators," *Opt. Lett.*, vol. 38, no. 9, pp. 1548–1550, May 2013, doi: 10.1364/OL.38.001548.
[37] P. Kharel, C. Reimer, K. Luke, L. He, and M. Zhang, "Breaking voltage–bandwidth limits in integrated lithium niobate modulators using micro-structured electrodes," *Optica*, vol. 8, no. 3, pp. 357–363, Mar. 2021, doi: 10.1364/OPTICA.416155.

Amr O. Ghoname (Graduate Student Member, IEEE) received the M.Sc. degree in electrical and computer engineering from Ain Shams University, Cairo, Egypt, in 2020. From 2016 to 2020, he was a Teaching and Research Assistant with Ain Shams University and as a part time optical design engineer at Si-ware Systems (SWS), Egypt. He is currently working toward the Ph.D. degree with the University of Illinois at Urbana–Champaign (UIUC), IL, USA. His research interests include integrated photonics, acoustic resonators, and hybrid microsystems for signal processing and sensing applications.

Mr. Ghoname was the recipient of the Best Paper Award from the 2018 IEEE, 35th National Radio Science Conference (NRSC), the 2022 Harriett and Robert Perry Fellowship Award, the 2023 Dr. Ok Kyun Kim Fellowship Award, and the 2024 Paul D. Coleman Outstanding Research Award from the Department of Electrical and Computer Engineering, UIUC.

Ahmed E. Hassanien received the Ph.D. degree in electrical and computer engineering from the University of Illinois at Urbana–Champaign (UIUC), Champaign, IL, USA, in 2022. From 2011 to 2015, he was a Full-Time Product Engineer with Si-ware Systems, Egypt. From 2015 to 2017, he was with Siemens EDA, Egypt, as an IC Design Consultant. He worked on energy harvesting from mechanical vibration using piezoelectric MEMS devices. His research interests include mechanical antennas, microwave filters, acoustic resonators, scanning mirrors, and integrated photonics.

Dr. Hassanien was the recipient of the 2018 Dr. Ok Kyun Kim Fellowship from the Department of Electrical and Computer Engineering, UIUC, and the 2020 Mavis Future Faculty Fellowship from the College of Engineering, UIUC.

Lynford L. Goddard (Senior Member, IEEE) received the Ph.D. degree in physics from Stanford, in 2005. His thesis topic was 1.5-micron gallium arsenide-based lasers. He conducted postdoctoral research with LLNL on photonic integrated circuits and sensors. He is currently the Edward C. Jordan Professor of electrical and computer engineering with the University of Illinois. He became the Founding Director of the Institute for Inclusion, Diversity, Equity, and Access in the Grainger College of Engineering in 2019 and the Associate Dean for Diversity, Equity, and Inclusion in 2021. His group fabricates, tests, and models photonic sensors, circuits, and instrumentation, develops novel device processing techniques, and applies quantitative phase microscopy for nanoscale science and for semiconductor wafer metrology. He is co-author of more than 250 publications and has 16 issued patents.

Dr. Goddard was an IEEE Photonics Journal Associate Editor during 2009–2014. He was the recipient tof the PECASE Award in 2010 and the AAAS Early Career Public Engagement Award in 2011. He is a Fellow of the SPIE and Optica.

Songbin Gong (Senior Member, IEEE) received the Ph.D. degree in electrical engineering from the University of Virginia, Charlottesville, VA, USA, in 2010. He is currently an Associate Professor and the Intel Alumni Fellow with the Department of Electrical and Computer Engineering and the Holonyak Micro and Nanotechnology Laboratory, University of Illinois at Urbana–Champaign, Urbana, IL, USA. His research interests include design and implementation of radio frequency microsystems, components, and subsystems for reconfigurable RF front ends. His research explores hybrid microsystems based on the integration of MEMS devices with photonics or circuits for signal processing and sensing.

Dr. Gong was the recipient of the 2014 Defense Advanced Research Projects Agency Young Faculty Award, 2017 NASA Early Career Faculty Award, 2019 UIUC College of Engineer Dean's Award for Excellence in Research, 2019 Ultrasonics Early Career Investigator Award, and 2022 IEEE Microwave Theory and Techniques (MTT) Society Microwave Prize. Along with his students and Postdoctoral Researcher, he was the recipient of the Best Paper Awards from the 2017 and 2019 IEEE International Frequency Control Symposium and the 2018, 2019, and 2020 International Ultrasonics Symposium, and won Second and Third Place in Best Paper Competition at the 2018 and 2020 IEEE International Microwave Symposium. He is a Technical Committee Member of the IEEE International Microwave Symposium and International Ultrasonic Symposium. He is currently an Associate Editor for IEEE TRANSACTIONS ON ULTRASONICS, FERROELECTRICS, AND FREQUENCY CONTROL, *Journal of Microelectromechanical Systems*, and *Journal of Microwaves*.